

The mechanism of a splash on a dry solid surface

Shreyas Mandre[†] and Michael P. Brenner

School of Engineering and Applied Sciences, Harvard University, Cambridge, MA 02138, USA

(Received 4 November 2010; revised 11 July 2011; accepted 22 September 2011;
first published online 28 November 2011)

From rain storms to ink jet printing, it is ubiquitous that a high-speed liquid droplet creates a splash when it impacts on a dry solid surface. Yet, the fluid mechanical mechanism causing this splash is unknown. About fifty years ago it was discovered that corona splashes are preceded by the ejection of a thin fluid sheet very near the vicinity of the contact point. Here we present a first-principles description of the mechanism for sheet formation, the initial stages of which occur before the droplet physically contacts the surface. We predict precisely when sheet formation occurs on a smooth surface as a function of experimental parameters, along with conditions on the roughness and other parameters for the validity of the predictions. The process of sheet formation provides a semi-quantitative framework for studying the subsequent events and the influence of liquid viscosity, gas pressure and surface roughness. The conclusions derived from this framework are in quantitative agreement with previous measurements of the splash threshold as a function of impact parameters (the size and velocity of the droplet) and in qualitative agreement with the dependence on physical properties (liquid viscosity, surface tension, ambient gas pressure, etc.) Our analysis predicts an as yet unobserved series of events within micrometres of the impact point and microseconds of the splash.

Key words: capillary flows, drops

1. Introduction

A high-speed droplet hitting a dry solid surface produces a splash. Despite over a century of study (from Worthington 1876), and detailed measurements of splashing thresholds (Levin & Hobbs 1971; Stow & Hadfield 1981; Bussmann, Chandra & Mostaghimi 2000), the fundamental mechanism underlying splashing on a dry solid surface is not understood. This was underscored by the recently unexpected discovery that the splash threshold depends on ambient air pressure (Xu, Zhang & Nagel 2005). As outlined by Rioboo, Tropea & Marengo (2001), Yarin (2006) and Deegan, Prunet & Eggers (2008), a host of different phenomena arise from droplet impact, going by the names of prompt splash, corona splash, etc. For the purposes of this paper, by ‘splash’ we mean the rapid event occurring when a droplet hits a surface, and without a discernible delay generates a sheet at very high speeds, which disintegrates into smaller droplets. The ejected sheet assumes the shape of a crown, and hence this phenomena is often called the corona splash. The disintegration of the sheet is an interesting problem in its own right, which has been studied extensively, see Keller &

[†] Email address for correspondence: shreyasmandre@gmail.com

Kolodner (1954), Fullana & Zaleski (1999), Song & Tryggvason (1999), Thoroddsen, Etoh & Takehara (2006), Dhiman & Chandra (2008), Zhang *et al.* (2010), and one we will not be concerned with here. Instead we focus on the origin of the liquid sheet which forms the corona and argue herein that a corona splash involves a sheet being ejected at very high speeds *before* the droplet contacts the surface. Although splashing, which is commonly defined as a breakup of the impacting drop, can occur from slower impacts, for the reasons described herein, the corona splash produces the fastest moving sheets and the smallest possible droplets. Sheet ejection has long been observed (Lesser & Field 1983), and heretofore there has been no plausible theoretical mechanism, and even modern high-speed visualization experiments have been unable to observe the initial steps of its formation.

The most prevalent mechanism for sheet formation invokes the compressibility of the liquid and the geometric singularity resulting from the locally parabolic shape of the interface at the instant of contact. As a consequence of this singularity, the contact line moves at speeds higher than the speed of sound in the liquid, leading to a shock wave (Lesser 1981; Lesser & Field 1983; Haller *et al.* 2003). When the contact line slows down below the speed of sound, this shock wave detaches from the contact line and causes ejection of a sheet. We have argued before (Mani, Mandre & Brenner 2010) that for millimetre sized droplets impacting at about 1 m s^{-1} , trapping of the surrounding air regularizes the geometric singularity by deforming the drop and keeping the liquid speed below the speed of sound. Hence the compressible-liquid mechanism cannot be underlying the mechanism of sheet ejection.

The role of air pressure in controlling splashing, as identified by Xu *et al.* (2005), has added an extra piece to the splashing puzzle. Many computational models (e.g. Harlow & Shannon 1967; Bussmann *et al.* 2000; Eggers, Fontelos & Josserand 2010; Yokoi 2011) do not take the surrounding air into account. Xu *et al.* (2005) also demonstrated a collapse of the splash threshold based on a scaling argument involving dynamic compressibility. They did not present a detailed mechanistic model for the process, and subsequent attempts (Schroll *et al.* 2010) to simulate the role of air have not yet exhibited a transition between splashing and spreading. Thus, while the scaling obtained by Xu *et al.* (2005) collapses their data, a mechanism for the process is still missing.

Here we describe a first-principles, theoretical description of what causes the sheet and the resulting corona splash, starting from the interaction of the liquid, solid and intervening gas. The critical stages determining whether splashing occurs are when the liquid is tens of nanometres from the surface, microseconds before contact. Our theory builds on our previous model (Mandre, Mani & Brenner 2009) that at low velocities the initial stages of liquid–solid impact result in a droplet spreading on a very thin layer of air; here we demonstrate that above a critical velocity, the liquid ejects a thin sheet before it contacts the surface. Sheet ejection arises from the competition between liquid inertia in the vicinity of the contact point and surface tension. When the sheet spreads on the air layer, there is no splash, but when it contacts the surface the resulting viscous forces can deflect the sheet upwards, causing a splash.

Splashing thus results from a two-stage process: the first stage causes the formation of a liquid sheet separated from the solid surface by a thin layer of air. We show this through the rigorous mathematical solution of the governing partial differential equations. The mathematical solution also furnishes us with quantitative predictions about the nature of sheet ejection.

The theory also predicts its own demise: if the surface roughness or the gas molecule mean-free path is larger than the air film thickness over which the sheet

is formed, the droplet contacts the surface before sheet formation; if a splash occurs, it will be far less violent. We present a quantitative map for how large a surface roughness is needed to disrupt violent splashes, as a function of droplet size, impact velocity and fluid parameters. If the sheet does form, the second stage involves deflecting it from the solid surface, mediated by contact of the sheet with the solid surface. We use these mathematical solutions to form a framework to semi-quantitatively predict the evolution of the ejected sheet and the underlying air layer beyond the inception of the sheet. Each of these stages can be interrupted by multiple physical effects, which accounts for the complexity of the phenomenon in our picture of the corona splash. In what follows we derive quantitative or qualitative predictions for each of these stages as a function of experimental parameters. Our theoretical framework quantitatively agrees with previous observations for the splash threshold, is qualitatively consistent with the dependence on liquid viscosity, air pressure and surface roughness (Xu *et al.* 2005), and also predicts an as yet unobserved series of events near the impact point, within microseconds of the splash.

2. Mathematical model for sheet formation

To analyse these dynamics, we model the drop as a two-dimensional planar incompressible fluid moving with velocity field $\mathbf{u}(x, t) = (u, v)$ governed by inviscid flow mechanics

$$\rho_l \mathbf{u}_t + \nabla \pi = -\rho_l \mathbf{u} \cdot \nabla \mathbf{u}, \quad \nabla \cdot \mathbf{u} = 0 \quad \text{for } y > h(x, t), \quad (2.1)$$

where π is the liquid pressure field and ρ_l the density of the liquid. The flow kinematically advects the liquid interface $y = h(x, t)$ according to $h_t + uh_x = v$, while the drop is forced to deform by the buildup of pressure in the gas film. On the other hand, the drop forces the air to drain from underneath it causing the buildup of pressure. This is described by the governing equations for the gas film, which simplify due to the thinness of the film to the well-known Reynolds lubrication equation modified for a compressible gas (Taylor & Saffman 1957)

$$12\mu (\rho h)_t - (\rho h^3 p_x)_x = -6\mu (\rho u h)_x \quad \text{and} \quad \pi - p = \sigma \kappa \quad \text{at } y = h(x, t), \quad (2.2)$$

where μ is the viscosity of the gas, p and ρ are the gas pressure and density respectively, σ is the interfacial tension and κ the interface curvature. The gas pressure and density are related by an equation of state $p = P_0 (\rho/\rho_0)^\gamma$, where P_0 and ρ_0 are the ambient pressure and density respectively, and the exponent γ is chosen to be 1 for isothermal and 1.4 for adiabatic compression. This forms a closed set of equations to model the near-impact dynamics.

The isothermal or adiabatic nature of the gas is determined by thermal considerations, which we show below to be the thermal properties of the liquid and the surface. If the surface can rapidly conduct heat on the time scale of 1 μs , then the gas can be maintained under isothermal conditions; on the other hand if the surface is a poor conductor of heat the adiabatic approximation is more appropriate. Moreover, the heating of the gas may also cause some of the liquid to evaporate, thus affecting the thermal budget. We conclude that for common materials, the isothermal approximation is more appropriate, hence we parametrized the gas using the exponent $\gamma = 1$.

We start our numerical simulations with the initial condition $h(x, t_{init}) = h_0 + x^2/2R$, $\mathbf{u} = (0, -V)$ and $p = P_0$ corresponding to an undeformed drop of radius R a sufficiently large distance h_0 from the surface at time $t_{init} = -h_0/V$. Our goal is to determine what happens to the interface as the droplet approaches the surface.

3. Non-dimensionalization and a reduced mathematical model

Initially, the surrounding gas has no effect; the effect of the dominant distorting forces, namely liquid inertia and gas viscosity, is felt when the lubrication pressure in the gas, which scales as $\mu VR/H^2$, becomes comparable to the pressure needed to decelerate the drop $\rho_l V^2 \sqrt{R/H}$, H being the thickness of the air film, μ being the viscosity of air and ρ_l the density of drop liquid. This provides the natural scale for the thickness of the air film to be $H = RSt^{2/3}$, where $St = \mu/\rho_l VR$ is the inverse Stokes number comparing the relative sizes of the gas viscous stresses to the droplet inertia. (The liquid viscosity can be neglected if it is sufficiently small, as explained in appendices A and B.) In typical experiments, St is about 10^{-6} – 10^{-5} and hence $H \ll R$. Dimensionally, the drop is within $\sim 1 \mu\text{m}$ of the surface in the last $\sim 1 \mu\text{s}$ before impact when it deforms. Both these dimensions and the scaling have been previously verified (Mani *et al.* 2010).

The small value of St implies that initially, the advection terms in (2.1)–(2.2) such as $\mathbf{u} \cdot \nabla \mathbf{u}$, $(\rho h)_x$ and uh_x scale a factor $St^{1/3}$ smaller than \mathbf{u}_t , $(\rho h)_t$ and h_t respectively. Physically, this means that the time scale of impact is so fast that the liquid particles are displaced a distance which is a factor $St^{1/3}$ smaller than the horizontal length scale. Thus the advection term in the material derivative is negligible compared to the time derivative. Similarly, the strength of the capillary pressure relative to the lubrication pressure is measured by $\delta = (\sigma/\mu V)St^{4/3}$, where σ denotes surface tension; this is approximately 10^{-5} – 10^{-4} in the parameter regime of interest and hence surface tension is initially negligible. This implies that the terms on the right-hand sides of (2.1)–(2.2) are initially small.

Thus the relevant scales for the impact process are found to be (Mandre *et al.* 2009; Mani *et al.* 2010)

$$\mathbf{u} = V\tilde{\mathbf{u}}, \quad \mathbf{x} = RSt^{1/3}\tilde{\mathbf{x}}, \quad h = RSt^{2/3}\tilde{h}, \tag{3.1a}$$

$$(p, \pi) = \frac{\mu V}{RSt^{4/3}}(\tilde{p}, \tilde{\pi}), \quad t = \frac{RSt^{2/3}}{V}\tilde{t}, \quad \rho = \rho_0\tilde{\rho}. \tag{3.1b}$$

Using these to non-dimensionalize, the equations become

$$\mathbf{u}_t + \nabla \pi = -St^{1/3}\mathbf{u} \cdot \nabla \mathbf{u}, \quad \nabla \cdot \mathbf{u} = 0, \tag{3.2}$$

$$\left. \begin{aligned} 12(\rho h)_t - (\rho h^3 p_x)_x &= -6St^{1/3}(\rho h)_x \\ \pi - p &= \delta\kappa \\ h_t - v &= -St^{1/3}uh_x \end{aligned} \right\} \text{ at } y = St^{1/3}h(x, t), \tag{3.3}$$

where $\kappa = h_{xx}/(1 + St^{2/3}h_x^2)^{3/2}$ is the non-dimensional interface curvature and we have dropped the tilde decoration. The equation of state for the gas becomes $p = \epsilon\rho^\gamma$, where $\epsilon = P_0RSt^{4/3}/\mu_g V$ is the ratio of the ambient pressure to the lubrication pressure and measures compressibility. Small ϵ means a very compressible gas, while for large ϵ the gas is incompressible.

As the drop compresses the gas film, the gas temperature rises. If $\epsilon \gg 1$, the compression, and consequently the temperature rise, is negligible; thus the precise value of γ used is irrelevant. For $\epsilon \lesssim 1$, this temperature rise penetrates a distance $\ell_{thermal} \sim St^{1/3}\sqrt{D_{thermal}R/V}$ into the solid surface and the liquid drop, where $D_{thermal}$ is the thermal diffusivity of the solid or the liquid. The relative thermal capacity of the thermal penetration layer to that of the gas is $B = \rho_{solid}C_{solid}\ell_{thermal}/\rho_0C_{gas}RSt^{2/3}$, where ρ_{solid} is the density of the solid, C_{solid} is its specific heat and C_{gas} is the specific heat

capacity of the gas, and it determines whether the gas may be treated as isothermal or adiabatic. If $B \gg 1$, the thermal capacity of the solid is much larger than that of the gas layer, and the solid provides a larger thermal reservoir to maintain the temperature of the gas layer. The isothermal approximation is appropriate in this situation. On the other hand, if $B \ll 1$, the solid layer is rapidly equilibrated to the gas temperature (or the thermal penetration depth is too small because the solid is insulating), making the adiabatic approximation appropriate. For conducting surfaces like copper, $B \approx 2.5 \times 10^4$, while for glass $B \approx 500$ and hence the isothermal approximation is applicable. We have not found a solid for which the adiabatic approximation is more appropriate, hence we only use $\gamma = 1$ in the simulations reported in this article.

Non-continuum effects are monitored by the inverse Knudsen number $Kn = h/\lambda$, where λ is the local mean-free path. In non-dimensional form,

$$Kn = \frac{h}{\lambda} = \frac{h}{\rho_0 \lambda_0 / \rho} = \frac{RSt^{2/3} \tilde{\rho} \tilde{h}}{\lambda_0} = Kn_0 \tilde{\rho} \tilde{h}, \tag{3.4}$$

where $Kn_0 = RSt^{2/3}/\lambda_0$. Since λ_0 increases with decreasing ρ_0 , $Kn_0 \propto \epsilon$ (we will also drop the tilde in (3.4)).

The initial velocity of the drop is uniform $(u, v) = (0, -1)$, and its initial vorticity is zero. By Kelvin’s circulation theorem for the inviscid approximation, this vorticity remains zero everywhere except in a boundary layer near the interface. In appendix B, we show that the inclusion of viscous effects in the boundary layer only plays the role of matching the shear stress at the interface and in doing so makes a small perturbation to the solution we describe. Since the vorticity in the bulk of the drop is zero, we can use a potential $\mathbf{u} = \nabla\phi$ to describe the velocity field in the drop. Mass conservation demands that

$$\nabla^2\phi = 0, \tag{3.5}$$

while the inviscid momentum conservation equation (3.2) reduces to the Bernoulli equation

$$\phi_t + \pi = -St^{1/3} \frac{|\nabla\phi|^2}{2}, \tag{3.6}$$

for $y > St^{1/3}h(x, t)$. The liquid pressure π is known at the interface, and hence (3.6) may be treated as an evolution equation for ϕ on the interface. If $f(x, t)$ is the value of ϕ on the interface, f satisfies the evolution equation

$$f_t + p = -St^{1/3} \frac{|\nabla\phi|^2}{2} - \delta \frac{h_{xx}}{(1 + St^{2/3}h_x^2)^{3/2}}. \tag{3.7}$$

The time-marching algorithm can then be roughly stated as below. We start with solving the Laplace equation for the potential and the fluid velocity everywhere for a given f on the boundary. Then we update the potential on the boundary using (3.7) to the new time step using the current p and ϕ . The current velocity is also used to kinematically advect the interface and to update the gas pressure according to (3.3). This then furnishes the new value of f , p and h on the interface to continue the time-stepping.

In order to solve for the potential in the drop, we exploit $St \ll 1$ and use perturbation methods to move the boundary of the domain from $y = St^{1/3}h(x, t)$ to $y = 0$. This is done by expanding the potential as $\phi = \phi_0 + St^{1/3}\phi_1 + \dots$, where at each

order $\nabla^2 \phi_k = 0$. The boundary conditions are

$$\phi_0 = f(x, t), \quad \phi_1 + h\phi_{0,y} = 0, \dots \quad \text{at } y = 0, \tag{3.8}$$

$$\phi_0 \rightarrow -y, \quad \phi_1 \rightarrow 0, \dots \quad \text{as } y \rightarrow \infty. \tag{3.9}$$

The Laplace equation for ϕ_k can be solved using a Hilbert transform. In particular, the required y -derivative of ϕ can then be written as $\phi_y = \phi_{0,y} + St^{1/3} \phi_{1,y} + \dots$, where

$$\phi_{0,y} = -1 + \mathcal{H}(f_x), \quad \phi_{1,y} = -\mathcal{H}((h\mathcal{H}(f_x))_x), \quad \text{etc.} \tag{3.10}$$

and \mathcal{H} denotes the Hilbert transform,

$$\mathcal{H}(g) = \frac{1}{\pi} \text{p.v.} \int_{-\infty}^{\infty} \frac{g(\xi)}{x - \xi} d\xi. \tag{3.11}$$

If we adopt the notation $\psi_y = \mathcal{H}(\psi_x)$ for $\psi(x, t)$, a one-dimensional model for p , f and h accurate to $St^{1/3}$ can be concisely written as

$$f_t + p = -\frac{St^{1/3}}{2} (f_x^2 + f_y^2) - \delta h_{xx}, \tag{3.12}$$

$$h_t - f_y + 1 = -St^{1/3} [(hf_x)_x + (hf_y)_y], \tag{3.13}$$

$$12(\rho h)_t - (\rho h^3 p_x)_x = -6St^{1/3} (\rho hf_x)_x. \tag{3.14}$$

These equations, along with the equation of state, are solved numerically subject to the initial conditions $h = h_0 + x^2/2$, $f = 0$ and $p = \epsilon$.

The numerical method is a slightly modified version of the method we previously used in the limit $St \rightarrow 0$ (Mani *et al.* 2010). We modify our previous method by adding the terms proportional to $St^{1/3}$ as inhomogeneities computed from the previous time step and treating them explicitly in the discretization. All other terms are discretized implicitly.

4. Self-similar approach to contact

The dynamics for a representative impact is shown in figure 1. Viscous forces in the gas resist the drainage of this film as pressure builds up in the centre of the film and the drop interface deforms into a dimple. (This dimple eventually evolves into a trapped bubble as observed by Chandra & Avedisian 1991 and Thoroddsen *et al.* 2005.) Additionally, as the drop attempts to contact the surface, at the rim of the dimple there is a rapid increase of gas pressure, liquid velocities and interface curvature (Mani *et al.* 2010; Mandre *et al.* 2009). The mechanics around this putative divergence holds the key to understanding droplet splashing.

We begin our analysis assuming incompressible flow in the gas, as is appropriate for air at 1 atm (Mani *et al.* 2010). At lower pressures, gas compressibility is important, as shown both in experiments (Xu *et al.* 2005) (see figure 2*d*) and in a theoretical description of the gas flow (Mani *et al.* 2010). The latter predicted that gas compressibility is important when the parameter ϵ is much smaller than 1. The compressibility becomes important at lower gas pressures, which we consider in § 7.

With these approximations, the solution to this model predicts that when the drop comes within about 1 μm of the surface, it is decelerated by the compressed air and a stagnation point develops near the centre (see figure 1). The liquid near the centre of the drop is diverted outwards and funnelled towards the periphery. This additional flux of liquid on the rim enhances the liquid velocities there and the rim of the drop is

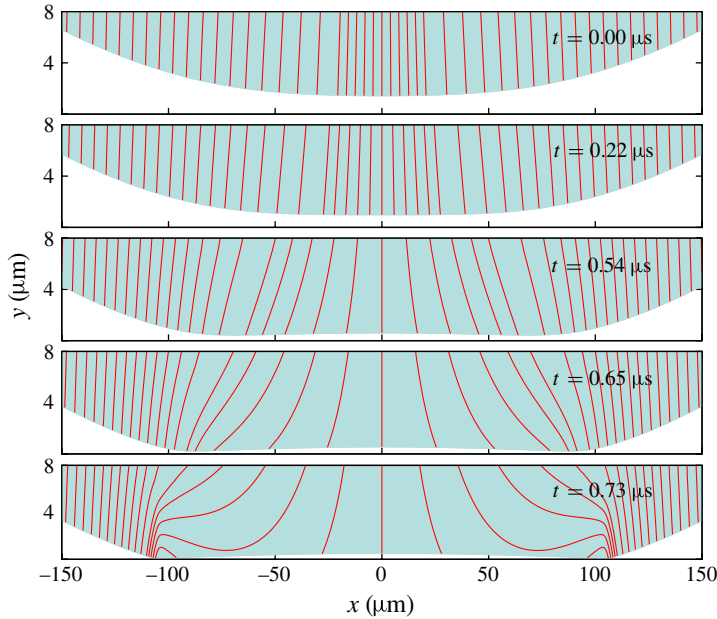


FIGURE 1. (Colour online available at journals.cambridge.org/flm) Dynamics occurring when a 1.7 mm radius ethanol drop moving at 3.7 m s^{-1} through air at 1 atm impacts on a rigid surface. The drop shape is shown shaded, while the curves show instantaneous streamlines of the flow in the drop. A bubble of air is trapped between the drop and the surface while the liquid velocity and interface curvature diverge at the rim of the bubble.

able to reach closer to the wall. In this process, the drop shape starts to develop sharp curvatures near the rim, and the drop velocities near the rim simultaneously grow. The air pressure underneath the rim grows to balance the enhanced liquid momentum and sustain the drainage of the air film. The same process repeats on smaller and smaller length and time scale as the rim gets pushed out further.

Mathematically, this corresponds to similarity solutions of the governing equations we had previously found (Mandre *et al.* 2009; Mani *et al.* 2010) by ignoring the small terms on the right-hand sides of (2.1)–(2.2).

When $St \ll 1$ and $\delta \ll 1$, the right-hand sides of (3.12)–(3.14) are small and can be neglected for the initial phases of impact. To leading order, the equations become

$$f_t + p = 0, \quad (4.1)$$

$$h_t - f_y + 1 = 0, \quad (4.2)$$

$$12(\rho h)_t - (\rho h^3 p_x)_x = 0. \quad (4.3)$$

We have previously conducted a detailed analysis of the solution of these equations (Mandre *et al.* 2009; Mani *et al.* 2010). These equations admit similarity solutions with decreasing length scale where the minimum air gap vanishes at a finite time t_0 as $h_{min} \propto (t_0 - t)^\alpha$; e.g. the self-similar form of the gas pressure is

$$p(x, t) = p_{max}(t) \Pi \left(\frac{x - ct}{\ell(t)} \right), \quad (4.4)$$

where Π is the self-similar profile, c is the speed with which this profile moves away from the centre of impact and $\ell(t)$ is the diminishing length scale. Let us first consider

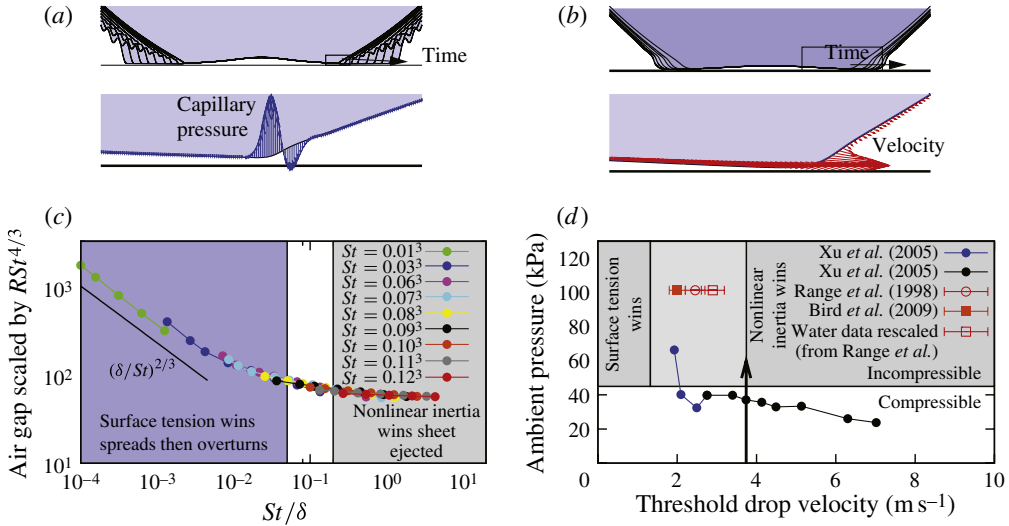


FIGURE 2. (Colour online) (a) Snapshots of the drop spreading on a thin film of air due to the surface tension (top). The capillary pressure resulting from the sharp curvatures developed on the interface (bottom) decelerate the drop and avert contact with the surface. (b) Snapshots of the interface overturning due to advection (top) and the instantaneous velocity of the interface leading to the overturning (bottom). (c) The dimensionless air gap as a function of $St/\delta = (\rho_l VR/\mu_g)^{1/3}(\mu_g V/\sigma)$, which measures the relative importance of advection to surface tension. For fast impacts, St/δ is large and the interface overturns ejecting a sheet. For slow impacts, St/δ is small and surface tension dominates causing the drop to spread on a thicker film of air as found before (Mandre *et al.* 2009). (d) Comparison with the experimental splash threshold for 1.7 mm radius ethanol drops on surface smooth up to at least 10 nm, with transition between spreading and sheet ejection in the incompressible limit for air. For ambient pressure larger than about 50 kPa, air can be considered to be incompressible (Mandre *et al.* 2009). The majority of splash thresholds are measured in this regime (Range & Feuillebois 1998; Bird, Tsai & Stone 2009). Xu *et al.* (2005) also reduced the air pressure, but they also found lower velocities for which the splash threshold velocity is almost independent of ambient pressure. These splash thresholds agree with the theoretical result, which predicts the threshold to lie on the crossover region $St/\delta \approx 0.1$ shown in (c).

the incompressible case $\epsilon \gg 1$ implying that $\rho \approx \text{constant}$ and only a small deviation from this constant density is able to accommodate the required pressure variation. The maximum relative pressure p_{max} , velocity u_{max} and curvature $h_{xx,max}$ diverge while the length scale ℓ approaches zero as

$$p_{max} \propto h_{min}^{-1/2}, \quad u_{max} \propto h_{min}^{-1/2}, \quad h_{xx,max} \propto h_{min}^{-2}, \quad \ell \propto h_{min}^{3/2}. \quad (4.5)$$

We call this the incompressible similarity solution.

If the diverging pressure becomes $O(\epsilon)$, the gas begins to compress significantly and the solution of (4.1)–(4.3) evolves to a different similarity solution, which we term the super-compressible similarity solution. While the self-similar profiles for the various functions are different, coincidentally the power-law exponents remain identical to those of the incompressible similarity solution. A salient feature of both these similarity solutions is their independence of the ambient pressure; it is only the transition between the two that depends on P_0 .

A third similarity solution is found for small $\epsilon \ll 1$, which corresponds to a small and very compressible ambient pressure. The equation of state in this case becomes $p = \epsilon \rho^\gamma \ll 1$ and mass conservation equation (4.3) in the air film becomes $\rho h \approx \text{constant}$. The similarity solution has the exponents

$$p_{max} \propto h_{min}^{-\gamma}, \quad u_{max} \propto h_{min}^{-\gamma}, \quad h_{xx,max} \propto h_{min}^{-1-2\gamma}, \quad \ell \propto h_{min}^{1+\gamma}. \quad (4.6)$$

We refer to this solution as the sub-compressible solution. The sub-compressible solution also transitions to the super-compressible similarity solution as the pressure builds up and cannot be neglected any more. Unlike the other two similarity solutions, the sub-compressible solution depends on the ambient pressure.

5. Stage I: sheet formation

Whether a droplet produces a thin sheet that results in a splash depends critically on what happens in the vicinity of the divergence. The key point is that the divergence implies that the initially negligible terms (the right-hand sides of (2.1)–(2.2), inertia, surface tension, liquid viscosity, gas compressibility and non-continuum effects) grow rapidly and potentially can take over the dynamics. The only effect whose neglect remains asymptotically valid near the divergence, as explained in appendix B, is liquid viscosity. The most dramatic effects are those of surface tension and nonlinear advection; depending on which is dominant, the divergence is regularized in different ways, leading to different types of sheet ejection. Owing to the vanishingly small length scale of the rim, the curvature in the azimuthal direction is overwhelmed by the curvature in the radial direction, and hence only a two-dimensional model is required to describe the dynamics.

Surface tension. Since the dimensionless curvature diverges as $1/h_{min}^2$, faster than gas pressure, it cannot be neglected in $\pi = p + \sigma \kappa$ when $\sigma \kappa \sim p$. Substituting the divergence laws (4.5), surface tension takes over the dynamics when $\delta/h_{min}^2 \sim 1/h_{min}^{1/2}$, or

$$h_{min} \sim 5\delta^{2/3}, \quad p_{max} = 0.8\delta^{-1/3}, \quad (5.1)$$

where the constants of proportionality are determined from the numerical solutions. Dimensionally, this scaling translates into $h_{min} \approx 5R\delta^{2/3}St^{2/3}$, as verified in figure 2(c). Computations also show that at this h_{min} the drop starts spreading on a thin layer of air, radiating capillary waves as shown in figure 2(a). Physically, the surface tension force due to the sharp curvature (shown in figure 2a) provides a sharp impulsive deceleration to the local drop velocity and obviates the need for the gas film to drain (Mandre *et al.* 2009). For a 1.7 mm ethanol drop moving at 1.5 m s⁻¹ ($\rho_l = 785 \text{ kg m}^{-3}$, $\sigma = 22 \text{ mN m}^{-1}$ and we use $\mu_g = 1.8 \times 10^{-5} \text{ Pa s}$, which corresponds to a Reynolds number $= \rho_l VR/\mu_l \approx 2000$, Weber number $= \rho_l V^2 R/\sigma \approx 140$) the air film is 25 nm thick.

Advection. For faster impacts, the high velocities localized in the vicinity of the rim cause the interfacial slope to diverge in finite time while the droplet is still a finite separation from the surface (figure 2b). This happens because a point on the interface near the rim moves faster than upstream points, amplifying the slope of the interface.

Mathematically, the advection terms such as $\mathbf{u} \cdot \nabla \mathbf{u}$, uh_x and $(\rho h)_x$ are initially negligible but grow faster than the time derivative terms \mathbf{u}_t , h_t and $(\rho h)_t$. In (3.12)–(3.14), these advection terms are seen to be proportional to $St^{1/3}$. If we again use the incompressible or the super-compressible divergence scalings, the time derivatives grow as $h_{min}^{-3/2}$, while the advection terms grow as h_{min}^{-2} . The advection terms can no longer be neglected when $St^{1/3}h_{min}^{-2} \approx h_{min}^{-3/2}$. This leads to the scaling estimate, $h_{min} \approx 60St^{2/3}$, where the constant of proportionality is found from numerical solutions

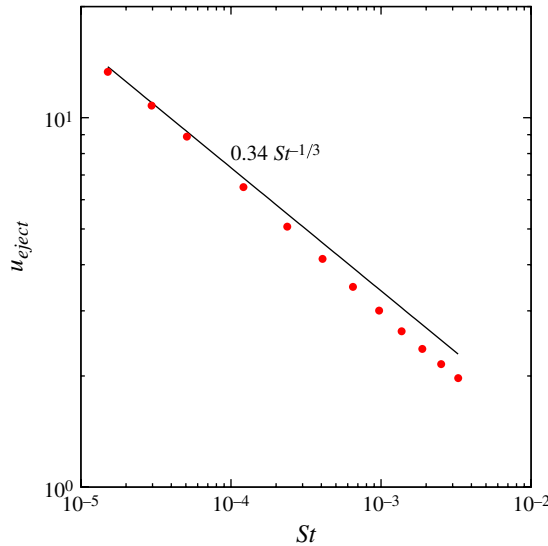


FIGURE 3. (Colour online) Sheet ejection velocity (dimensionless) as a function of St in the incompressible limit. The line shows the prediction based (5.2a) and the dots the numerical solution.

shown in figure 2(c). The effect of the advection terms is to cause the interface slope to diverge in finite time.

Although our approximations break down once the interfacial slope becomes too steep, the mechanism of slope amplification that occurs here is mathematically identical to that observed in overturning ocean waves and in low-viscosity droplet breakup (Chen, Notz & Basaran 2002). The diverging slope is therefore an indication of sheet ejection. The fact that the slope divergence can occur on top of a finite air film implies that the initial stages of sheet ejection occur before liquid–solid contact. A similar steepening of the slope is considered to be underlying splashing on liquid layers (Yarin & Weiss 1995), but milliseconds after the drop had merged with the liquid layer.

We can also predict the exact instant in time when the advection terms begin to dominate the dynamics, along with the maximum horizontal velocity on the interface and the radial location of the diverging slope. The overturning occurs at $t \approx 7.6$ in time units non-dimensionalized according to (3.1), where $t = 0$ occurs when the undeformed drop would have touched the surface in the absence of air. The location of the overturning is $x \approx 5$ in non-dimensional units.

The velocity at the instant of overturning can also be found by substituting the scale for h_{min} when advection becomes dominant in the divergence law (4.5) for velocity. This gives the ejection velocity to be $0.34St^{-1/3}$. This prediction is compared with the numerical solution in figure 3. Written in terms of dimensional variables, these quantities are

$$h_{min} \sim 60RSt^{4/3}, \quad \mathbf{u}_{eject} \sim 0.34VSt^{-1/3}, \quad (5.2a)$$

$$r_{eject} \sim 5RSt^{1/3}, \quad t_{eject} \sim 7.6RSt^{2/3}/V, \quad (5.2b)$$

where \mathbf{u}_{eject} is the initial velocity of the sheet, r_{eject} the rim radius at which the sheet is ejected, t_{eject} the time of sheet ejection and the prefactors are determined from

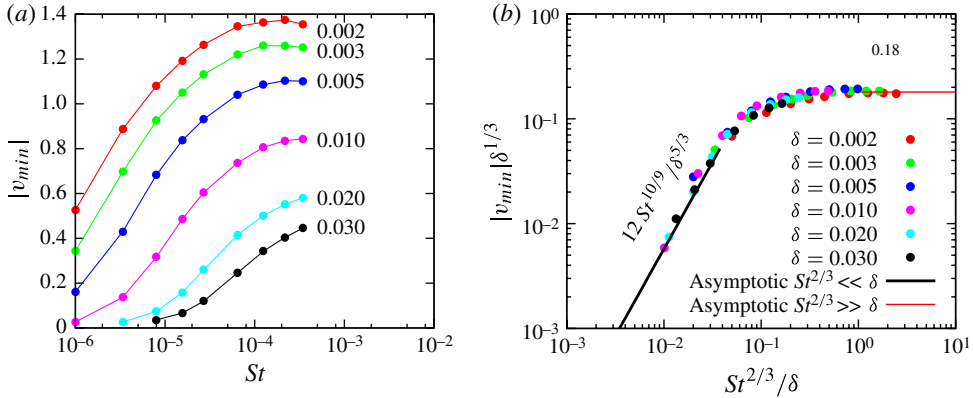


FIGURE 4. (Colour online) (a) The magnitude of the vertical velocity (dimensionless) v_{min} at the location where $h = h_{min}$ and the instant of overturning, as a function of St for difference δ . (b) Same data as in (a), but collapsed onto a universal curve by plotting $v_{min}\delta^{1/3}$ against $St^{2/3}/\delta$. It can be seen from this graph that as δ increases, the approach velocity decreases.

numerical solutions of (2.1)–(2.2). Our ability to predict the prefactors in (5.2) is due to the universal nature of the similarity solution leading to the initial divergence (Mani *et al.* 2010). These estimates allow detailed quantitative predictions of when the sheet is initially ejected: for example for a 1.7 mm radius ethanol droplet moving at 3.74 m s^{-1} (Xu *et al.* 2005) (Reynolds number ≈ 5000 , Weber number ≈ 850) we predict that a liquid sheet emanates from a point $100 \mu\text{m}$ from the centre of impact, at a speed 83 m s^{-1} and at $t = 0.8 \mu\text{s}$ measured relative to the instant when the centre of the drop would have touched the surface in the absence of the surrounding gas. The gas film is $1.6 \mu\text{m}$ thick at the centre, but only 7 nm thick at the point of ejection.

It is worth remarking that even in the surface-tension-dominated regime, during the spreading of the droplet on the air film, eventually the advection terms grow in magnitude sufficiently to cause overturning and sheet ejection. However, the conditions under which the sheet is ejected are different, and much less violent in the surface-tension-dominated regime. Owing to the decelerating action of capillary forces in the surface-tension regime, the interface velocity is almost horizontal behind the spreading front. This is shown in figure 4(a), which plots the vertical velocity of the interface v_{min} at the location where $h = h_{min}$ and at the instant of sheet ejection for various values of St and δ . As can be seen from this figure, as δ increases (i.e. surface tension grows), v_{min} decreases. A better understanding of the dependence of v_{min} on St and δ can be achieved by scaling v_{min} with $\delta^{-1/3}$ and plotting it against $St^{2/3}/\delta$. In these rescaled variables, the data in figure 4(a) collapse onto a single curve, as shown in figure 4(b). For small δ (i.e. negligible surface tension), the collapsed curve approaches an asymptotic value of $v_{min}\delta^{1/3} \sim 0.18$, which shows that as surface tension increases the vertical velocity decreases. Similarly, for large δ , $v_{min} \sim 12St^{10/9}/\delta^2$, showing again that the vertical velocity decreases, even approaches zero asymptotically, with increasing surface tension. Thus, at the moment of overturning in the surface-tension-dominated regime, the interface has smaller vertical velocity and thus much less propensity to drain the air out and contact the surface.

A universal transition. Which takes over first, advection (sheet ejection) or surface tension (spreading on an air film)? This is determined by the effect that sets in at the largest h_{min} . To determine this we compare h_{min} from the surface-tension

regime (5.1) with the advection regime (5.2); the effects are comparable when $h_{min}^{advection} = 60St^{2/3} \sim h_{min}^{surface\ tension} = 5\delta^{2/3}$, or $St/\delta \sim (12)^{-3/2} = 0.024$. Mathematically, when $St \gg \delta$, advection becomes dominant before surface tension and the interface overturns ejecting a sheet. While when $St \ll \delta$, the curvature becomes dominant before the advection and the drop spreads on a thin film of air. Thus, the two possibilities can be combined in a universal curve described by

$$\frac{h_{min}}{St^{2/3}} = \chi \left(\frac{St}{\delta} \right), \tag{5.3}$$

where $\chi(\xi) \approx 60$ for large ξ and $\chi(\xi) \approx 5\xi^{-2/3}$ for small ξ , as shown in figure 2(c).

To test this prediction, we solved (2.1)–(2.2) numerically for a wide range of St and δ . For each set of parameters, we find the air gap at which there is a transition to either the regime dominated by surface tension (in which the film spreads on an air layer) or advection (in which a sheet is ejected). If we plot the dimensionless transition thickness $h_{min}/St^{2/3}$ against $St/\delta = (\rho_l VR/\mu_g)^{1/3}(\mu_g V/\sigma)$, we find that data collapse, as shown in figure 2(c). There is a critical velocity corresponding to a critical St/δ above which sheet ejection occurs, and below which the film spreads on a thicker air layer. Figure 2(c) shows that the critical velocity corresponds to $St/\delta \approx 0.05$ – 0.2 , close to the range anticipated by the simple argument above. Dimensionally, this translates to the critical velocity for sheet ejection

$$V_{threshold} = C \left(\frac{\sigma^3}{\mu_g^2 \rho_l R} \right)^{1/4}, \quad 0.1 < C < 0.3. \tag{5.4}$$

The uncertainty in the prefactor C is related to gradual transition between the two regimes; $C > 0.3$ corresponds to the inertial asymptotic regime, while $C < 0.1$ corresponds to the surface-tension-dominated asymptotic regime.

Even if the drop starts to spread due to surface tension, eventually advection becomes dominant and causes the interface to overturn. The nature of this delayed overturning is different from the direct overturning due to advection stated above. Firstly, the overturning with surface tension occurs with a larger air gap, as shown in (5.3) and evidenced in figure 2(c). There is another factor lowering the propensity to contact for the surface-tension-dominated regime. This is measured by the vertical velocity at the point of minimum air film thickness v_{min} . The numerically calculated vertical velocity of approach is shown in figure 4 for various values of St and δ . The dependence of v_{min} on the two parameters can be collapsed onto a single curve by plotting $v_{min}\delta^{1/3}$ versus $St^{2/3}/\delta$. We have not found the detailed explanation for such a collapse, but it is evident from the raw data in figure 4(a) and the scaled data in figure 4(b) that the vertical velocity of approach diminishes with increasing surface tension. In the surface-tension regime, the capillary pressure decelerates the fall of the drop thus reducing the vertical velocity. The air film drains proportionally slowly and thus contact may be delayed until much later.

Owing to these two differences between the two regimes, it is plausible that the drop contacts the surface shortly after sheet ejection in the regime dominated by advection, while in the surface-tension-dominated regime the air film drainage is significantly slower and contact is postponed.

Non-continuum effects. Our analysis thus far has assumed that the gas can be described with continuum hydrodynamics, including the no-slip boundary condition at the solid surface. When the mean-free path of the gas is of order the gas film

thickness, the no-slip boundary condition is violated (Maxwell 1879), and there is slip of the gas at the solid surface. This decreases the wall resistance to flow, facilitating drainage of the gas and the rupture of the film. The potential relevance of this effect is quantified by the inverse Knudsen number $Kn = h_{min}/\lambda$, where λ is the local mean-free path of the gas molecules. Studies (Gopinath, Chen & Koch 1997) have shown that when $Kn < 10$ the wall resistance to flow reduces even below Maxwell's predictions and facilitates contact.

For the two examples considered above, numerical solutions of (2.1)–(2.2) show that a 1.7 mm ethanol droplet moving at 1.5 m s^{-1} skates on a 25 nm air film, compressed to about 30 atm, and consequently the mean-free path is reduced to about 2 nm, implying $Kn \sim 12$. In contrast, at a speed of 3.74 m s^{-1} , the air film thickness is only 7 nm when the sheet is ejected, whereas the mean-free path is reduced to $\approx 1.4 \text{ nm}$, implying $Kn \sim 5$. The continuum theory therefore breaks down at higher impact velocities. We expect this to lead to the rupture of the air film and hence liquid–solid contact, soon after the overturning.

6. Stage II: sheet deflection

We have thus far described a mechanism for the formation of a thin fluid sheet, with the ejected sheet launching with a velocity parallel to the substrate. Splashing requires the sheet to be deflected away from the solid surface. The prediction that sheet ejection at high impact velocities is accompanied by a breakdown in the continuum theory and hence liquid–solid contact suggests a natural mechanism for such deflection to occur (figure 5).

Once contact occurs, a viscous boundary layer will develop near the region of contact. Viscous drag decelerates the liquid in contact with the surface and thus provides an abrupt resistance to the horizontal flow of the liquid coming from the centreline of the drop. To conserve flux of volume, the horizontal flow must be diverted away from the surface. In other words, the viscous boundary layer has a wall-normal velocity, which scales as the wall-parallel velocity times the aspect ratio of the boundary layer (we caution the reader that we are not invoking boundary layer separation, but simply boundary layer growth). This wall-normal velocity directs individual fluid particles away from the wall. If this diverted flow is directed into the newly formed lamella, the lamella takes off from the surface and forms a corona. If this diverted flow is too far from the lamella, or for some reason unable to cause the lamella to lift off, the drop spreads smoothly on the surface. Within this framework, the deceleration of the drop by capillary pressure in the surface-tension-dominated regime obviates the need for the air to drain out from the film, avoids contacts and thus arrests splashing. In general, splashing can be arrested by any mechanism that delays liquid–solid contact (e.g. trapping more gas beneath the droplet, or modifications of intermolecular interaction between the liquid and the surface).

To demonstrate that this mechanism of splashing is consistent with previous observations, we compare the threshold velocity in (5.4) with the splash threshold. The experimentally observed threshold velocity for ethanol drops on smooth surfaces agrees with the prediction, as seen in figure 2(d), for $P_0 \gtrsim 50 \text{ kPa}$ when air can be treated as incompressible. The prediction also allows us to rescale the threshold velocity for water drops (Range & Feuillebois 1998) by a factor of $(\sigma_{water}/\sigma_{ethanol})^{3/4} (\rho_{water}/\rho_{ethanol})^{-1/4}$ to agree with ethanol drops of same size. Thus, our results indicate that the splash threshold at ambient pressure arises from

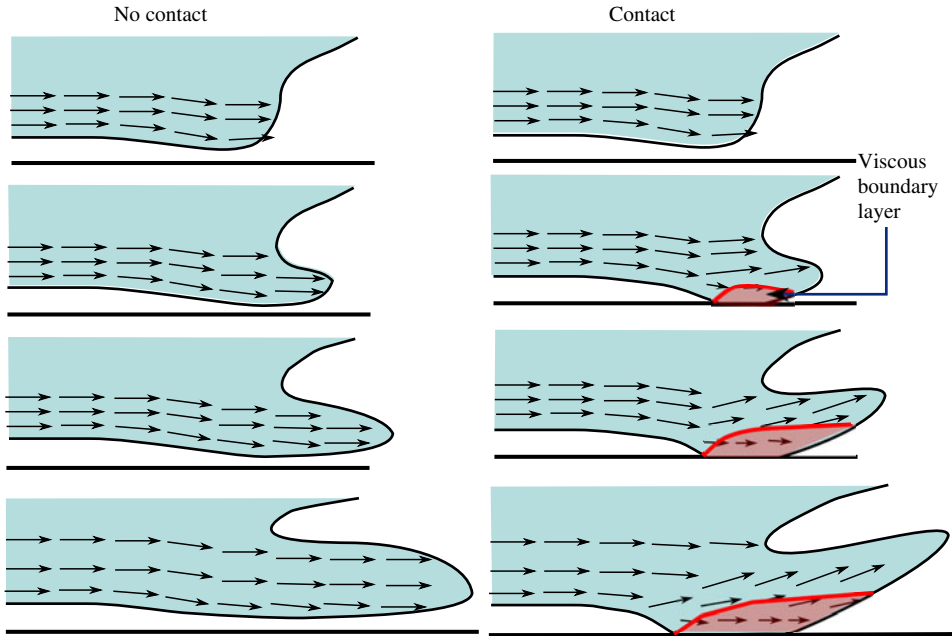


FIGURE 5. (Colour online) A schematic summarizing the postulated mechanism for the lift-off of the lamella when contacting the surface. (a) A sequence starting from the instant of overturning (top frame) for the case when the gas film remains intact and the drop does not contact the surface. The lamella then smoothly spreads along the surface. (b) A sequence of snapshots for the case when the gas film ruptures or otherwise allows contact. Viscous drag from the no-slip condition at the contacted region causes the liquid in a boundary layer to decelerate substantially. The liquid behind this region is then diverted upwards and forced to flow away from the surface to conserve volume. If this diverted liquid enters the lamella, the lamella lifts off and leads to a crown.

the competition between surface tension forces and inertia, with inertia promoting splashing through sheet ejection and surface tension suppressing it.

7. Compressibility

All the dynamics described so far are modified by reducing the ambient pressure. For example, the location and instant of overturning are modified as the gas pressure is reduced. For low ambient pressure, the non-dimensional time of sheet ejection is $t_{eject} = 18\epsilon^{1/3}$, and the non-dimensional x -location of sheet ejection is $20\epsilon^{1/2}$, as shown in figure 6. The transition between incompressible and compressible regimes occurs for $\epsilon \approx 0.1$, which translates to an ambient pressure of 0.5 atm for a 1.7 mm radius ethanol drop impacting at 3.74 m s^{-1} .

While reducing the ambient pressure changes the quantitative criteria for spreading, sheet ejection and the threshold for balance between surface tension and inertia, it more severely modifies the continuum nature of the gas. Intuitively, one expects that reducing the ambient pressure increases the mean-free path of the gas molecules and thus enhances non-continuum effects and promotes splashing. While this expectation is upheld for asymptotically large ($P_0 \gtrsim 10 \text{ atm}$) and asymptotically small ($P_0 \lesssim 0.1 \text{ atm}$) ambient pressures, we find that it is not true between these two regimes. In this intermediate regime, decreasing P_0 actually increases the amount of gas trapped in the

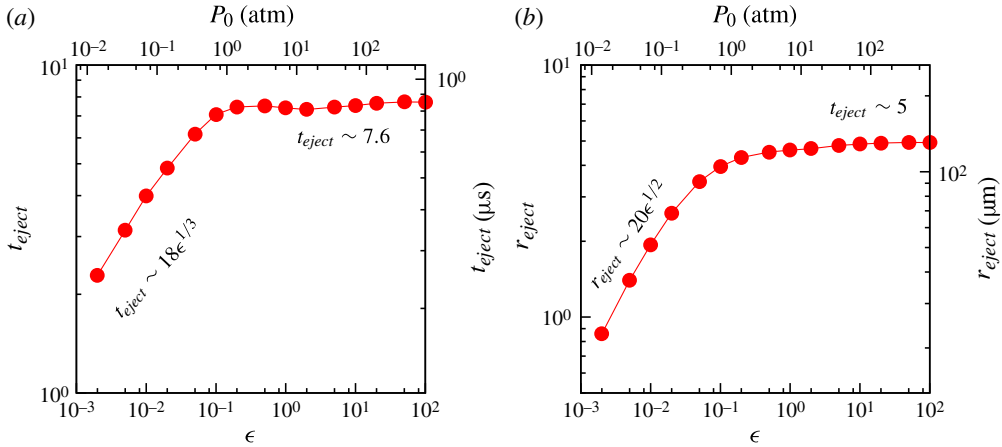


FIGURE 6. (Colour online) (a) The non-dimensional time instant of sheet ejection as a function of ϵ . (b) The non-dimensional radius of the rim at which the sheet is ejected plotted as a function of ϵ . For an 1.7 mm ethanol drop moving at 3.74 m s⁻¹, the corresponding dimensional value is shown on the right axis of both panels vs the dimensional ambient pressure on the top axis.

gas film, avoids contact of the liquid with the wall and thus suppresses splashing. To see this quantitatively, we consider the dependence of Kn on ambient pressure P_0 , in both the asymptotically compressible and incompressible limits, for a 1.7 mm ethanol droplet impacting at 3.74 m s⁻¹.

The treatment of compressibility and non-continuum effects is most transparent in dimensional variables, and we transform back to the dimensional form of equations in this section. The local mean-free path follows from (3.4) as

$$Kn_{min} = \frac{(\rho h)_{min}}{\lambda_0 \rho_0}. \tag{7.1}$$

Note that $Kn_{min} \propto (\rho h)_{min}$, the minimum mass of gas trapped in the air film per unit area. Thus the continuum nature of the gas is maintained for longer if more mass is trapped in the gas film.

In the incompressible regime, i.e. at large ambient pressure P_0 , the gas density and hence the mean-free path are fixed. Thus the mass trapped and Kn depend only on h_{min} at the instant of overturning. Substituting h_{min} from (5.2) into (7.1) implies $Kn = 60RS t^{4/3} / \lambda_0$. Since λ_0 itself depends on the ambient pressure, to interpret this expression we substitute λ_0 in terms of a standard value at 1 atm, denoted by subscript atm. This translates to

$$Kn_{min} \sim \frac{60RP_0St^{4/3}}{\lambda_{atm}P_{atm}}. \tag{7.2}$$

This implies that Kn_{min} scales linearly with atmospheric pressure P_0 at high pressures. The validity of this regime can be estimated from the next-order correction to the pressure; at the instant of overturning and sheet ejection $p = P_0(1 + 0.08/\epsilon St^{1/3})$. This gives the leading-order correction to Kn_{min} and the deviation from the leading-order behaviour occurs for $\epsilon = 0.08St^{-1/3}$. For an 3.4 mm diameter ethanol drop impacting at 3.7 m s⁻¹, the asymptotic regime is valid for $P_0 > 10$ atm.

Different considerations lead to the pressure dependence of Kn_{min} at small P_0 . In this regime, the drainage term in (2.2) becomes negligible and the dominant balance becomes $(\rho h)_t = 0$ or $\rho h = \text{constant}$. This means that a certain constant amount of gas remains trapped in the film, and due to (7.1), Kn_{min} also remains constant. To determine this constant value, we have to estimate the amount of gas trapped in the film, which is determined by the early dynamics of the impact (Mandre *et al.* 2009). When the drop is sufficiently far from the interface, the gas behaves incompressibly and the gas pressure builds up as $\mu VR/h_{min}^2$. The gas is incompressible as long as this pressure is less than the ambient pressure but starts to compress when the two become comparable. This transition determines the amount of gas that becomes trapped to be $\rho h = 5.6\rho_0 (\mu VR/P_0)^{1/2}$, the constant being determined from numerical solutions. Substituting this in (7.1) leads to $Kn_{min} = 5.6 (\mu VR/P_0)^{1/2} / \lambda_0$. Again substituting λ_0 in terms of quantities at 1 atm, Kn_{min} asymptotically depends on P_0 as

$$Kn_{min} \sim \frac{5.6 (\mu VR P_0)^{1/2}}{P_{atm} \lambda_{atm}}. \quad (7.3)$$

Next-order corrections predict the regime to be valid for $P_0 < 0.1$ atm. Thus Kn_{min} asymptotically decreases with decreasing gas pressure in both the large- P_0 and small- P_0 limit.

Figure 7 plots these two asymptotic behaviours at large and small P_0 as black lines with parameters chosen for a 1.7 mm ethanol drop moving at 3.74 m s^{-1} , which correspond to the black arrow in figure 2(d). What is striking is that the high-pressure limit overshoots the low-pressure limit; continuity therefore implies that there must be an intermediate regime in which Kn_{min} increases by a factor of at least 6 as the pressure is decreased from 10 atm to 0.1 atm. Indeed, the red asterisk plots the Kn_{min} corresponding to the numerical simulation carried out above, and lies precisely between the two asymptotes. The red dotted line indicates an interpolation of the two asymptotes passing through the numerically computed point. Physically, as the ambient pressure is reduced, the air film compresses rather than draining and this traps more air, thus increasing Kn . The increased Kn_{min} suppresses non-continuum effects, in particular drainage of the gas film, and thus delays contact between the drop and the solid. Splashing is thereby suppressed. We can also make a quantitative prediction for the threshold pressure: a critical Kn_{min} of 10 implies that the threshold ambient pressure for air is approximately 0.4 atm, quite close to the measured splash threshold (figure 7).

Repeating this procedure for different droplet parameters (St, δ) would give predictions of the threshold splash pressure as a function of these parameters. We do not carry out this analysis here owing to the demanding nature of the required computations. The extremely small size of St necessitates a very fine grid; since inversion of the Hilbert transform in the governing equations is performed with a uniform grid in our current numerical algorithm, this pushes the limits of our computational resources.

8. Discussion and experimental tests

The theory outlined here explain a number of different experimental observations and suggests new experiments for further validation:

(a) *Splash threshold velocity*: numerically, (5.4) considered as the threshold for splashing gives good agreement with experimental measurements reported in the literature. For example, for approximately a 1.7 mm radius ethanol droplet, (5.4)

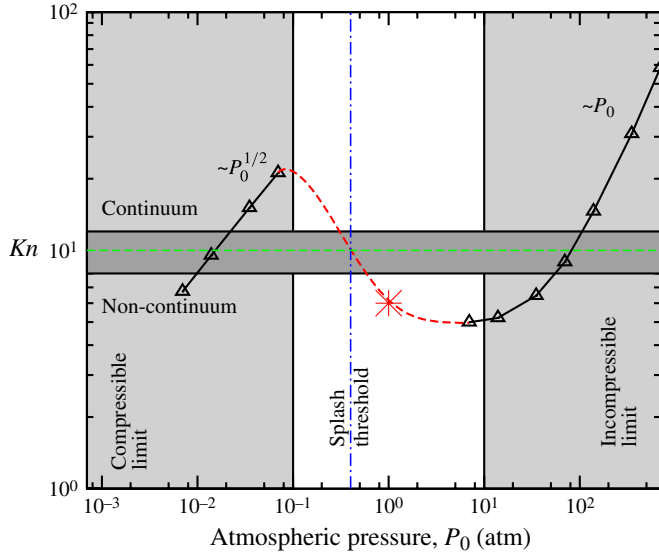


FIGURE 7. (Colour online) The inverse Knudsen number $Kn = h/\lambda$ at the instant of sheet ejection as a function of the ambient pressure at a constant impact speed $V = 3.74 \text{ m s}^{-1}$ shown by the arrow in figure 2(d). For asymptotically large and small ambient pressure (the black curve with triangles), Kn decreases with decreasing P_0 . However, in the intermediate regime the schematic red dashed curve connecting the two asymptotic regimes shows that Kn grows with P_0 signifying that more air gets trapped as the ambient pressure is reduced. The asterisk is a result of numerical solution of (3.2)–(3.3) in neither of the asymptotic regimes. As the ambient pressure decreases, the air in the trapped film finds it easier to compress than to drain out resulting in this counter-intuitive behaviour. The horizontal band with the dashed line shows the approximate boundary between continuum and non-continuum behaviour (Gopinath *et al.* 1997).

gives a value between 1.25 and 3.75 m s^{-1} , while the experimentally observed value is about 2.4 m s^{-1} (Range & Feuillebois 1998; Xu *et al.* 2005; Bird *et al.* 2009). The threshold velocity for a water drop of about the same size ($\rho_l = 1000 \text{ kg m}^{-3}$, $\sigma = 72 \text{ mN m}^{-1}$) is between 3 and 8.6 m s^{-1} , while the experimentally observed value is 6.6 m s^{-1} . These points are plotted in figure 2(d) (the experimental threshold for water is plotted by rescaling it by a factor $(\sigma_{\text{water}}/\sigma_{\text{ethanol}})^{3/4} (\rho_{\text{water}}/\rho_{\text{ethanol}})^{-1/4}$ derived from (5.4), so that it can be compared with ethanol). We are unable to determine at this time exactly where in the range given by (5.4) the splash threshold lies; the precise value will depend on the quantitative details of sheet deflection.

Direct comparison between published experimental correlations and our model is difficult because none of the published correlations include the physical parameters we include in our model. None of the investigations prior to 2005 includes any properties of the surrounding gas, while the work by Xu and co-workers after 2005 (Xu *et al.* 2005; Xu 2007) invokes a speed of sound in the gas. In our analysis, the gas viscosity is one of the prime parameters, the dependence on liquid viscosity and gas molecular weight is qualitative and the speed of sound plays no role. Thus, at this stage the comparison can only be limited to a discussion of which parameters play a role in the dynamics.

The drop velocity and the drop radius appear in every correlation and are also varied significantly in the experiments. The liquid density and surface tension have also appeared in the correlations but the tested experimental range of variation is limited.

For example, the correlation by Mundo, Sommerfeld & Tropea (1995) reads

$$\frac{\rho_l^{0.75} V^{1.25} R^{0.75} \mu_l^{0.25}}{\sigma^{0.5}} = \text{constant}, \quad (8.1)$$

while our (5.4), when cast in the same form, reads

$$\frac{\rho_l V^4 R \mu_g^2}{\sigma^3} = \text{constant}. \quad (8.2)$$

The dependence on R , V , ρ and σ is qualitatively consistent between the two. Consistency to this degree exists with all previously published correlations which can be found, for example, summarized by Rein & Delplanque (2008).

(b) *Air Pressure*: as explained above, our theory of splashing explains the experimentally observed (Xu *et al.* 2005) critical ambient pressure in the range of 0.2–0.5 atm to suppress splashing.

(c) *Surface roughness*: rough surfaces are ubiquitous and the roughness comes in a range from atomically smooth 0.1 nm to the size of the drop. Surface roughness facilitates contact by introducing singular features in the boundary of the flow domain. Our theory predicts that roughness on different scales affects splashing differently. Even roughness on the nanometre scale can influence splashing behaviour.

Roughness on a scale larger than a few microns, especially manufactured anisotropic roughness like micro-pillars (Xu 2007), modifies the initial approach of the drop as the air layer is drained through the pillars. This initial approach without the manufactured roughness is described in detail by Mani *et al.* (2010), and this analysis can be used to estimate the scale of roughness which can influence the approach. The roughness provides additional channels for air to drain and thus facilitates contact. Since this contact occurs in the very early phases of the impact, i.e. before the formation of a high-velocity sheet, and possibly even before the droplet deforms, splashing is suppressed. On the time scale of 1 ms a sheet is nevertheless formed (Harlow & Shannon 1967; Schroll *et al.* 2010), simply due to mass conservation, but is much slowed down by viscous forces. This slower sheet can be deflected by the textured roughness to induce splashing (Josserand *et al.* 2005). We direct the reader to Xu (2007) for a discussion on the view that the splashing with surface roughness larger than a few microns leads to a prompt splash. One consequence of this picture is that the drop will spread anisotropically on a textured surface, because the resistance to air escaping through the texture is anisotropic. This predicts that the shape of the spreading sheet will mimic the texture of the surface; we refer the reader to Reyssat *et al.* (2010) and Tsai *et al.* (2010) for a supporting account of this picture.

Even the smoothest surface is rough on the molecular scales. One relevant scale for roughness to influence the dynamics of drop impact considered in this paper is the air film thickness. Since the air film thickness can be in nanometres, even the smoothest surfaces may appear rough for splashing. Unfortunately, the roughness of commonly available ‘smooth’ surfaces varies considerably. One may obtain molecularly smooth single-crystal sapphire for a splashing substrate; however we are unaware of splashing experiments carried out on such surfaces. During the peer-review process, a referee upon their own initiative contacted a major glass manufacturing company and received a roughness specification of 300 nm for common window-pane glass. The editor of this manuscript kindly solicited measurements of the surface roughness of common substrates using atomic force microscopy measurements of various glass surfaces, which reveal a peak roughness of approximately 10 nm (J. R. T. Seddon 2011 and L. A. Tran 2011, personal communications). Our own collaborators, also using atomic force

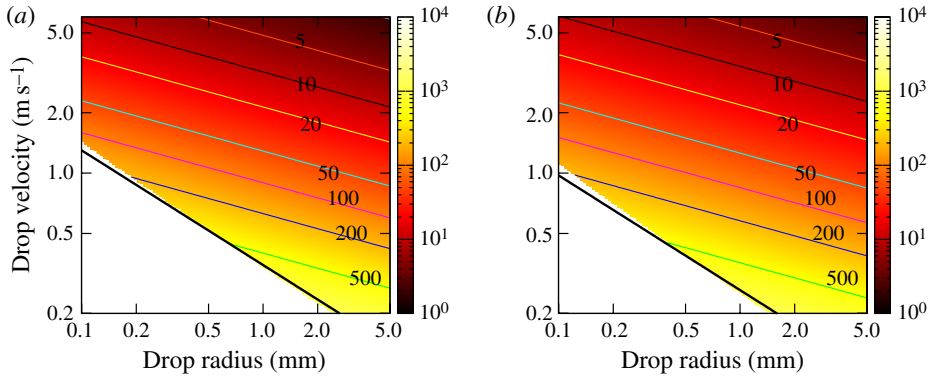


FIGURE 8. (Colour online) Scale of roughness in nanometres that can influence the impact of (a) a water and (b) an ethanol drop during sheet ejection as a function of the drop radius and velocity. Below the solid black curve, the $\delta \ll 1$ approximation is violated, and thus drop deformation is resisted by surface tension instead of droplet inertia. Above the solid black curve, intensity denotes the air film thickness at the instant of sheet ejection computed from (5.3). The thin lines denote contours of constant air film thickness of the value denoted by the adjoining label. This thickness provides an estimate for the scale of wall roughness to be significant.

microscopy, independently measured the peak roughness of commonly available glass slides to be approximately 10 nm (M. Chon, H. van Lengerich & K. S. Breuer, 2011, personal communication). A variety of measurements on commonly available soda-lime glass slides reveals a roughness of approximately 10 nm or 50 nm depending upon the chemical treatment and the manufacturing date (North *et al.* 2009). In previous experiments on splashing, various metals were polished smooth up to a smoothest of 10 nm (Vander Wal, Berger & Mozes 2006). In order to facilitate the verification of the analysis presented in this paper, and given the wide variation in the roughness of materials used for the splashing substrate, we present a bound on the scale of roughness as a function of the experimental parameters below which our analysis is valid. Of course, the informed reader may be able to predict the dynamics even if their roughness is larger than this bound, as we do below.

Roughness on the smaller scale promotes contact (Cawthorn & Balmforth 2010) and hence can induce splashing after a high-speed liquid sheet is formed. Any roughness on a scale comparable to the air film thickness thus has the potential to rupture the air film and accelerate contact. The thickness of the air gap at the moment the sheet is ejected is plotted in figure 8. It can be seen in this figure that, for example, a 2 mm diameter drop impacting at 1 m s^{-1} ejects a sheet when the air film is 80 nm thick. If the surface has a peak roughness of 10 nm, then the air film will not be ruptured on account of the roughness, but if the roughness is 300 nm, the air film will not stay intact.

Figure 8 explains why the splash threshold depends on surface roughness as small as 10 nm (see figure 9 in Range & Feuillebois 1998). The splash threshold for a 1.8 mm radius water drop on a glass surface of roughness 15 nm was measured by Range & Feuillebois (1998) to be 4.4 m s^{-1} . For these parameters, the air film thickness of 5 nm can be read from figure 8, which is comparable to the scale of the roughness. In § 9, we provide more examples of the effect of surface roughness.

(d) *Molecular weight of gas*: the continuum nature of the gas is governed by the mean-free path of the gas molecules, which depends on the gas molecular weight. Hence the splash threshold should also vary with the molecular weight, consistent with observations (Xu *et al.* 2005).

(e) *Liquid viscosity*: firstly, our theory applies only if the viscous forces in the liquid are overwhelmed by the liquid inertia, as outlined in appendix A. Once dominated by the liquid inertia, the viscous forces remain negligible and are not amplified by the self-similar divergence in (4.5) and (4.6). Thus small liquid viscosity can only play a role once the liquid touches the solid surface and is decelerated by the no-slip boundary condition in the deflection stage.

In the deflection stage, this mechanism for splashing also predicts a non-monotonic dependence on the liquid viscosity. Our mechanism predicts that liquid viscosity plays a role only after contact, in controlling the boundary layer at the surface that deflects the sheet. The boundary layer develops to a thickness given by ν_l/U_{eject} , where ν_l is the kinematic viscosity of the liquid and U_{eject} is the velocity scale of the liquid near the point of contact. This thickness is approximately 10 nm for a liquid like ethanol. This is smaller than the thickness of the sheet when it first appears, which simulations show to be about 50 nm. We anticipate that both the boundary layer and sheet thicknesses grow rapidly with time and hence a separate detailed analysis of the processes is required to make quantitative predictions. Qualitative understanding can still be obtained and is consistent with experimentally observed non-monotonic dependence on liquid viscosity (Xu 2007). Increasing the viscosity increases the thickness of the boundary layer, thereby diverting the fluid more efficiently and also utilizing more and more the thickness of the lamella. However, for too large a viscosity (~ 10 cP), the boundary layer becomes so thick that the diverted fluid begins increasingly to miss the lamella. In these more viscous cases, we expect the ejected lamella to be deflected much later by entraining air at or near the contact line (Rein & Delplanque 2008).

(f) *Direct visual observation*: current visualization techniques are too slow for directly observing the series of events described in this paper. The fastest videos of the impact process show that a sheet is ejected (i.e. the interface becomes multivalued near the point of impact) without any discernible delay from the instant of impact. Most experimental observations of the ejected sheet are made with a temporal resolution of no more than 10 μs (Mongruel *et al.* 2009; de Ruiter, Pepper & Stone 2010). Fast cameras providing frame rates of 10^6 frames s^{-1} are available and have been used to study the ejecta sheet for droplet impact on liquid films (Thoroddsen 2002; Thoroddsen *et al.* 2011), but not on dry solid surfaces. The events that we predict in this article, however, occur faster than 1 μs .

We expect advances in imaging to make these observations possible in the near future (Thoroddsen, Etoh & Takehara 2008). The relevant time and length scales for the sheet formation process presented in (5.2) could then be readily compared with observations and provide a quantitative verification of the splashing mechanism. Indirect visualization using interference or total internal reflection on a microsecond time scale could also help verify the mechanism.

9. Representative illustrations of the framework

Here we apply the framework outlined in this paper to available experimental observations in order to illustrate its application. This section was inspired by a referee's review, who wanted to know if the results of this paper could be applied to,

and whether they agreed with, the observations of Mongruel *et al.* (2009) and Rioboo, Marengo & Tropea (2002). We also add an example from the experiments by Vander Wal *et al.* (2006).

(a) Mongruel *et al.* (2009). Their figure 1(a) shows multiply exposed snapshots of a 4.85 mm diameter water drop impacting a surface at 1.73 m s^{-1} . Using the viscosity (1 cSt), density (1000 kg m^{-3}) and surface tension (72 mN m^{-1}) of water, we first verify that inertia dominates over viscous forces in the drop (as clarified in appendix A, $Re = 8391$ means that this is true), as well as over the surface tension forces ($\delta = 1.6 \times 10^{-4}$). This means that the analysis in the first stage of impact (the sheet formation) is quantitatively applicable. Then we calculate the threshold velocity from (5.4) for drop spreading versus sheet ejection to be between 2.65 and 7.87 m s^{-1} . Since the experimental impact velocity is smaller, on a smooth surface the drop would spread before ejecting a sheet. The thickness of the air film the drop would spread on can be calculated from the dimensional version of (5.1) to be 9.5 nm. Similarly, the pressure in the air film can also be estimated to be 25.7 atm, which corresponds to the mean-free path of the compressed gas film of 2.5 nm, so approximately 4 mean-free paths fit within the thickness of the film. These numbers essentially find their origin in the solution of the Navier–Stokes equations.

The roughness of the surface that Mongruel *et al.* (2009) reported was 10–50 nm. On account of this roughness being larger than the air film thickness, we would expect the drop to contact the surface before it starts to spread. The liquid viscosity makes its influence felt through the no-slip boundary condition and slows down the rapid speed inside the drop. There is no opportunity for the interface to overturn and a sheet to be ejected according to the mechanism elucidated in §5. Sheet ejection nevertheless occurs due to mass conservation, but is postponed to hundreds of microseconds after these events. Since contact occurs before the high-speed sheet is ejected, we expect there to be no splashing immediately by our mechanism, which is consistent with observations of Mongruel *et al.* (2009).

(b) Rioboo *et al.* (2002). Their figure 3 shows multiply exposed snapshots of a 2.73 mm diameter drop of 10 cSt glycerine at an impact speed of 0.96 m s^{-1} on a glass surface. The roughness of the surface was not mentioned, but a range of roughness between 3 nm and $120 \mu\text{m}$ was mentioned encompassing all the experiments reported in that work. In the absence of a better estimate, we assume that the roughness of the glass surface that Rioboo *et al.* (2002) used for the experiment in figure 3 was about 3 nm. The Reynolds number for this impact is 131 and δ is 1.3×10^{-3} , which suggests that inertia dominates over liquid viscosity and surface tension. The threshold velocity from (5.4) for drop spreading versus sheet ejection is between 3 and 9 m s^{-1} . The experimental speed is much slower than that, so we conclude that the drop spreads on a thin film of air before it ejects a sheet. The air film thickness can be calculated using the dimensional version of (5.1) to be about 50 nm. The pressure in the air film is 4 atm, which corresponds to a mean-free path of 17 nm. Thus about 3 mean-free paths of the air molecules fit within the film thickness. Since this impact occurs in the spreading regime, the vertical velocity of the interface is reduced to zero behind the spreading front. The sheet ejection occurs $6.2 \mu\text{s}$ after impact. The first exposure Rioboo *et al.* (2002) make is $365 \mu\text{s}$ after impact, and then an overturned interface is seen. A reasonable verification is not possible due to the slow imaging in the experiments.

The mean-free path of the air molecules is about 3 times smaller than the air film thickness, and the roughness is about 15 times smaller. While continuum theory is on the verge of breaking down, the action of surface tension to stop the interface from

falling postpones contact. Thus, we predict that the air film will remain intact on the time scale of impact in our analysis. Thus we expect the drop to spread smoothly and not splash immediately upon impact, which is consistent with what was observed.

(c) Vander Wal *et al.* (2006). Their tables 2, 3 and 4 list a series of experiments on a 2 mm diameter drop impacting on an aluminium surface with a mirror polish. The roughness of the surface was less than 10 nm. As an example, let us consider a butanol drop (density 810 kg m^{-3} , viscosity 3.5 cSt and surface tension 20 mN m^{-1}) impacting at 2.17 m s^{-1} . For a 2 mm butanol drop the spreading-sheet ejection threshold according to (5.4) is between 1.3 and 4 m s^{-1} . Thus the drop velocity of 2.17 m s^{-1} is in the transition region, and one has to use the universal curve in figure 2(c). Doing so, one finds that a sheet is ejected when the air film thickness is 18 nm. The gas pressure is 15 atm, which corresponds to a mean-free path of 4 nm. Thus a high-speed sheet will be ejected in this case before contact.

However, continuum theory is on the verge of being violated with about 5 mean-free paths of the air molecules fitting in the air film thickness. Also, while the roughness is lower than the air film thickness, one can estimate the magnitude of the vertical velocity at the instance of overturning using data from figure 4 to be about 8 m s^{-1} . Thus, we expect the drop interface to keep approaching the solid surface even after sheet ejection and soon to contact the surface. This process in our mechanism predicts an immediate rapid splash. A splash is experimentally reported by Vander Wal *et al.* (2006) for this case, but is not classified as either occurring immediately after the impact or much later.

To summarize, this article proposes through a combination of asymptotic analysis and numerical simulations that splashing occurs through a two-step process. The first step involves the ejection of a thin liquid sheet before the drop touches the surface; we show that this occurs microseconds before contact when the droplet is separated from the solid surface by tens of nanometres, provided the surface is smoother than this separation. The second stage of splashing requires this sheet to be deflected away from the solid surface, a process that requires contact with the surface and the development of a viscous boundary layer. The two-staged process leads to a splashing threshold with complicated dependence on surface roughness, liquid viscosity, gas pressure and gas molecular weight. While some of the details in the second stage remain to be uncovered, our analysis is quantitatively consistent with experiments performed to date. Further details can be probed in future experiments.

Acknowledgements

We acknowledge support from the National Science Foundation through the Division of Mathematical Sciences, the Harvard MRSEC and the Kavli Institute for Bionano Science and Technology at Harvard. We thank the referees for a spirited debate and their constructive criticism. We also gratefully acknowledge the JFM editorial support for undertaking an independent initiative to measure surface roughness of glass plates.

Appendix A. Limits on validity due to liquid viscosity and surface tension

In this article, we have assumed a dominant balance between lubrication theory in the gas and inertial dynamics in the liquid. For a sufficiently viscous liquid, this dominant balance could be violated at the stage of droplet deformation. In other words the lubrication pressure in the gas layer $\mu VR/H^2$ could be balanced by a viscous stress $\mu_l V/\sqrt{RH}$ that resists deformation of the liquid interface, instead of the inertial

pressure scale $\rho_l V^2 \sqrt{R/H}$. The condition on liquid viscosity to be dominated by inertia is

$$\mu_l \ll \rho_l VR \quad \text{or} \quad Re = \frac{\rho_l VR}{\mu_l} \gg 1. \quad (\text{A } 1)$$

This condition identifies the non-dimensional combination of parameters that govern the competition between liquid inertia and viscosity; for $Re \ll 1$ liquid viscosity dominates, but for $Re \gg 1$, the liquid inertia dominates. In the absence of a numerical solution including both the liquid inertia and viscosity, it is not possible to determine the precise value of the transition Re . Typical values of Re are about $O(1000)$ for the less viscous liquids (water, ethanol, isopropyl alcohol, etc. which have viscosities close to 1 cSt), and are $O(100)$ for liquids that are 10 times as viscous.

Similarly, the limits of validity of our analysis require that surface tension be initially negligible (although the governing equations are valid for arbitrary surface tension), which translate to $\delta \ll 1$.

Appendix B. Effect of liquid viscosity in Stage I

A thin boundary layer of thickness $L\sqrt{v/UL}$ is formed in the liquid near the interface to accommodate the tangential stress. The velocity (u_b, v_b) in the boundary layer satisfies

$$\rho_l(u_{b,t} + u_b u_{b,x} + v_b u_{b,y}) = -\pi_x + \mu_l u_{b,yy}, \quad (\text{B } 1)$$

$$u_{b,x} + v_{b,y} = 0. \quad (\text{B } 2)$$

The tangential stress condition is $\mu_l u_{b,y} = -\mu h p_x / 2$ at $y = h$, where $y = h$ is the interface location and p is the lubrication pressure in the gas. This boundary layer flow is matched in the far field to the potential flow (u, v) that we have solved for in detail; i.e. $(u_b, v_b) \rightarrow (u, v)$ as $y \rightarrow \infty$. Since the interface is advected by the local velocity $h_t + u_b h_x = v_b$, the extent to which (u_b, v_b) differ from (u, v) determines whether the tangential stress effect is important or not.

We have numerically solved (B 1)–(B 2) coupled with our simulations (2.1)–(2.2), and found that while (u, v) diverge as a result of the similarity solution described earlier, the difference $(u_b - u, v_b - v)$ does not grow as rapidly. This is essentially due to the fact that the tangential stress in the gas is non-zero in only a small region of length $\ell(t)$ where the self-similar dynamics are active. Since this region moves away from the centre of impact at a constant speed c_{rim} , successive surface elements are only exposed to a growing shear stress for a vanishing time. The net momentum transferred may be estimated as shear stress \times time of exposure $= \mu h p_x \ell / c_{rim}$, which scales as $h_{min}^{1/2}$ and vanishes to zero as the singularity is approached. Since the duration of exposure to the stress vanishes more rapidly than the shear stress grows, the effect of the tangential stress becomes successively weaker compared to the inviscid dynamics.

REFERENCES

- BIRD, J. C., TSAI, S. S. H. & STONE, H. A. 2009 Inclined to splash: triggering and inhibiting a splash with tangential velocity. *New J. Phys.* **11**, 063017.
- BUSSMANN, M., CHANDRA, S. & MOSTAGHIMI, J. 2000 Modelling the splash of a droplet impacting a solid surface. *Phys. Fluids* **12**, 3121–3132.
- CAWTHORN, C. J. & BALMFORTH, N. J. 2010 Contact in a viscous fluid. Part 1. A falling wedge. *J. Fluid Mech.* **646**, 327–338.

- CHANDRA, S. & AVEDIKIAN, C. T. 1991 On the collision of a droplet with a solid surface. *Proc. Math. Phys. Sci.* **432** (1884), 13–41.
- CHEN, A. U., NOTZ, P. K. & BASARAN, O. A. 2002 Computational and experimental analysis of pinch-off and scaling. *Phys. Rev. Lett.* **88** (17), 174501.
- DEEGAN, R. D., PRUNET, P. & EGGERS, J. 2008 Complexities of splashing. *Nonlinearity* **21**, C1–C11.
- DHIMAN, R. & CHANDRA, S. 2008 Rupture of radially spreading liquid films. *Phys. Fluids* **20**, 092104.
- EGGERS, J., FONTELOS, M. A., JOSSEKAND, C. & ZALESKI, S. 2010 Drop dynamics after impact on a solid wall: theory and simulations. *Phys. Fluids* **22**, 062101.
- FULLANA, J. M. & ZALESKI, S. 1999 Stability of a growing end rim in a liquid sheet of uniform thickness. *Phys. Fluids* **11**, 952–954.
- GOPINATH, A., CHEN, S. B. & KOCH, D. L. 1997 Lubrication flows between spherical particles colliding in a compressible non-continuum gas. *J. Fluid Mech.* **344**, 245–269.
- HALLER, K. K., POULIKAKOS, D., VENTIKOS, Y. & MONKEWITZ, P. 2003 Shock wave formation in droplet impact on a rigid surface: lateral liquid motion and multiple wave structure in the contact line region. *J. Fluid Mech.* **490**, 1–14.
- HARLOW, F. H. & SHANNON, J. P. 1967 The splash of a liquid drop. *J. Appl. Phys.* **38**, 3855.
- JOSSEKAND, C., LEMOYNE, L., TROEGER, R. & ZALESKI, S. 2005 Droplet impact on a dry surface: triggering the splash with a small obstacle. *J. Fluid Mech.* **524**, 47–56.
- KELLER, J. B. & KOLODNER, I. 1954 Instability of liquid surfaces and the formation of drops. *J. Appl. Phys.* **25** (7), 918–921.
- LESSER, M. B. 1981 Analytic solutions of liquid-drop impact problems. *Proc. R. Soc. Lond. A* **377**, 289–308.
- LESSER, M. B. & FIELD, J. E. 1983 The impact of compressible liquids. *Annu. Rev. Fluid Mech.* **15**, 97–122.
- LEVIN, Z. & HOBBS, P. V. 1971 Splashing of water drops on solid and wetted surfaces: hydrodynamics and charge separation. *Phil. Trans. R. Soc. Lond. A* **269**, 555–585.
- MANDRE, S., MANI, M. & BRENNER, M. P. 2009 Precursors to splashing of liquid droplets on a solid surface. *Phys. Rev. Lett.* **102** (13), 134502.
- MANI, M., MANDRE, S. & BRENNER, M. P. 2010 Events before droplet splashing on a solid surface. *J. Fluid Mech.* **647**, 163–185.
- MAXWELL, J. C. 1879 On stresses in rarified gases arising from inequalities of temperature. *Phil. Trans. R. Soc. Lond. A* **170**, 231–256.
- MONGRUEL, A., DARU, V., FEUILLEBOIS, F. & TABAKOVA, S. 2009 Early post-impact time dynamics of viscous drops onto a solid dry surface. *Phys. Fluids* **21**, 032101.
- MUNDO, C. H. R., SOMMERFELD, M. & TROPEA, C. 1995 Droplet–wall collisions: experimental studies of the deformation and breakup process. *Intl J. Multiphase Flow* **21** (2), 151–173.
- NORTH, S. H., LOCK, E. H., KING, T. R., FRANEK, J. B., WALTON, S. G. & TAITT, C. R. 2009 Effect of physicochemical anomalies of soda-lime silicate slides on biomolecule immobilization. *Analyt. Chem.* **82** (1), 406–412.
- RANGE, K. & FEUILLEBOIS, F. 1998 Influence of surface roughness on liquid drop impact. *J. Colloid Interface Sci.* **203** (1), 16–30.
- REIN, M. & DELPLANQUE, J. P. 2008 The role of air entrainment on the outcome of drop impact on a solid surface. *Acta Mechanica* **201**, 105–118.
- REYSSAT, M., RICHARD, D., CLANET, C. & QUÉRÉ, D. 2010 Dynamical superhydrophobicity. *Faraday Discuss.* **146**, 19–33.
- RIOBOO, R., MARENGO, M. & TROPEA, C. 2002 Time evolution of liquid drop impact onto solid, dry surfaces. *Exp. Fluids* **33** (1), 112–124.
- RIOBOO, R., TROPEA, C. & MARENGO, M. 2001 Outcomes from a drop impact on solid surfaces. *Atomiz. Sprays* **11** (2), 155–166.
- DE RUITER, J., PEPPER, R. E. & STONE, H. A. 2010 Thickness of the rim of an expanding lamella near the splash threshold. *Phys. Fluids* **22**, 022104.
- SCHROLL, R. D., JOSSEKAND, C., ZALESKI, S. & ZHANG, W. W. 2010 Impact of a viscous liquid drop. *Phys. Rev. Lett.* **104** (3), 34504.

- SONG, M. & TRYGGVASON, G. 1999 The formation of thick borders on an initially stationary fluid sheet. *Phys. Fluids* **11**, 2487–2493.
- STOW, C. D. & HADFIELD, M. G. 1981 An experimental investigation of fluid flow resulting from the impact of a water drop with an unyielding dry surface. *Proc. R. Soc. Lond. A* **373**, 419–441.
- TAYLOR, G. I. & SAFFMAN, P. G. 1957 Effects of compressibility at low Reynolds number. *J. Aeronaut. Sci.* **24**, 553.
- THORODDSEN, S. T. 2002 The ejecta sheet generated by the impact of a drop. *J. Fluid Mech.* **451**, 373–381.
- THORODDSEN, S. T., ETOH, T. G. & TAKEHARA, K. 2006 Crown breakup by marangoni instability. *J. Fluid Mech.* **557** (-1), 63–72.
- THORODDSEN, S. T., ETOH, T. G. & TAKEHARA, K. 2008 High-speed imaging of drops and bubbles. *Annu. Rev. Fluid Mech.* **40**, 257–285 ISSN 0066-4189.
- THORODDSEN, S. T., ETOH, T. G., TAKEHARA, K., OOTSUKA, N. & HATSUKI, Y. 2005 The air bubble entrapped under a drop impacting on a solid surface. *J. Fluid Mech.* **545**, 203–212.
- THORODDSEN, S. T., THORAVAL, M. J., TAKEHARA, K. & ETOH, T. G. 2011 Droplet splashing by a slingshot mechanism. *Phys. Rev. Lett.* **106** (3), 34501 ISSN 1079-7114.
- TSAI, P., VAN DER VEEN, R. C. A., VAN DE RAA, M. & LOHSE, D. 2010 How micropatterns and air pressure affect splashing on surfaces. *Langmuir* **26** (20), 16090–16095.
- VANDER WAL, R. L., BERGER, G. M. & MOZES, S. D. 2006 Droplets splashing upon films of the same fluid of various depths. *Exp. Fluids* **40** (1), 33–52.
- WORTHINGTON, A. M. 1876 On the forms assumed by drops of liquids falling vertically on a horizontal plate. *Proc. R. Soc. Lond. A* **25**, 261–272.
- XU, L. 2007 Liquid drop splashing on smooth, rough, and textured surfaces. *Phys. Rev. E* **75** (5), 56316.
- XU, L., ZHANG, W. W. & NAGEL, S. R. 2005 Drop splashing on a dry smooth surface. *Phys. Rev. Lett.* **94**, 184505.
- YARIN, A. L. 2006 Drop impact dynamics: splashing, spreading, receding, bouncing. *Annu. Rev. Fluid Mech.* **38**, 159–192 ISSN 0066-4189.
- YARIN, A. L. & WEISS, D. A. 1995 Impact of drops on solid surfaces: self similar capillary waves and splashing as a new type of kinetic discontinuity. *J. Fluid Mech.* **283**, 141–173.
- YOKOI, K. 2011 Numerical studies of droplet splashing on a dry surface: triggering a splash with the dynamic contact angle. *Soft Matt.* **7**, 5120–5123.
- ZHANG, L. V., BRUNET, P., EGGERS, J. & DEEGAN, R. D. 2010 Wavelength selection in the crown splash. *Phys. Fluids* **22**, 122105.